MCNP6 CODE DEVELOPMENT FOR ONE DIMENSIONAL POSITION SENSITIVE THERMAL NEUTRON DETECTORS

A Thesis

by

JOSEPH G. FUSTERO

Submitted to the Office of Graduate and Professional Studies of
Texas A&M University
in partial fulfillment of the requirements for the degree of

MASTER OF SCIENCE

Chair of Committee,	Ryan G. McClarren
Co-Chair of Committee,	Delia Perez-Nunez
Committee Members,	Marvin L. Adams
	Daniel G. Melconian
Head of Department,	Yassin A. Hassan

December 2017

Major Subject: Nuclear Engineering

ABSTRACT

The development of position sensitive thermal neutron detectors (PSD's) began soon after the initial development of early model thermal neutron detectors. One dimensional (1D) PSD's report not only neutron counts but the axial position of the neutron interaction within the detector gas volume. These detectors maintain a high level of fidelity except when the neutron interaction takes place close to the gas-shell boundary.

The use of PSD's in order to characterize the spatial distribution of the thermal neutron field will become more commonplace as the technology has become less expensive. These experiments, however, must be validated against simulation results in order to assure their quality. The stochastic radiation transport code MCNP6 was used in order to provide these simulation results due to its large user base and its compatibility with the Parallel Deterministic Transport (PDT) code.

It was found that it is possible to use MCNP6 to accurately simulate 1D PSD's without heavily editing the source code. MCNP6 was used to simulate both the position of the neutron interaction as well as the predicted detector response due to the charge generation resultant of this interaction. This was done by writing a TALLYX modification to the default energy deposition F6 tally for charged particles which result from a neutron interaction. Additionally, it was found that using the PTRAC particle tracing utility for events contributing to the F6 tally for the cell corresponding to the detector gas volume was also appropriate for determining the location of the neutron

interaction and the corresponding detector response due to charge collection on the anode wire.

These simulations were run for a line detector test problem, a modified already completed impurity model experiment, and a future localized source experience. For all of these simulations the expected spatial distribution (including symmetries) and notable physical features (wall effect due to surface leakage of heavy charged particles) was observed. The computational expense did not differ significantly from a simulation using the default MCNP6 tallies.

DEDICATION

This thesis is dedicated to Michael Crichton who can be blamed for inspiring the naive author of this thesis to pursue a career in science and engineering.

ACKNOWLEDGEMENTS

I would like to thank Dr. McClarren for his patience while advising me on this project. As a newcomer to computational science, I often posed questions that would seem obvious to the more experienced mind, yet he would always take the time to address my concerns in detail.

I would also like to thank Dr. Thomas Conroy and Dr. Sophit (Bo) Pongpun, the experimentalists working with our group's position sensitive detector. Our numerous conversations offered me insight into how to accurately model all of the physical phenomena which contribute to the experimental detector response.

Additionally, I would like to thank Dr. Adams for initially proposing this project and providing some of the initial assumptions. And I would like to thank the other members of my committee, Dr. Melconian and Dr. Perez-Nunez for their feedback and questions throughout the process of performing this research.

Finally, I would like to thank Kermit Bunde (Department of Energy) for assisting me in compiling MCNP6 using modern compilers.

CONTRIBUTORS AND FUNDING SOURCES

Contributors

This work was supported by a thesis committee of Dr. Ryan McClarren [advisor], Dr. Delia Perez-Nunez [co-advisor], and Dr. Marvin Adams of the Department of Nuclear Engineering and Dr. Daniel Melconian of the Department of Physics.

Insightful discussions with Dr. Thomas Conroy and Dr. Sophit Pongpun both of the Texas A&M Engineering Experiment Station helped with developing Chapter 3. Additional discussions with Kermit Bunde of the Department of Energy served as precursors to the code development outlined in Chapter 4.

All other work conducted for the thesis was completed by the student independently.

Funding Sources

This project was funded by the Center for Exascale Radiation Transport (CERT). CERT was founded by a grant from the National Nuclear Security Agency (NNSA), specifically under the Predictive Science Academic Alliance Program (PSAAP-II).

NOMENCLATURE

CERT	Center for Exascale Radiation Transport
HCP	Heavy Charged Particle
MCNP	Monte Carlo n-Particle
PSD	Position Sensitive Detector
SR	Stopping Range
SRIM	Stopping Range of Ions in Matter

TABLE OF CONTENTS

Page

LIST OF FIGURES

FIGURE Page

LIST OF TABLES

TABLE Page

1. INTRODUCTION

The Texas A&M CERT research group has recently acquired a 3 m long position sensitive BF_3 thermal neutron detector. This detector will be eventually taken to the Nuclear Science Center in order to perform experiments characterizing the spatial distribution of the thermal neutron flux coming from an AmBe neutron source.

In order to provide assurance that the results acquired by the experimentalists are reasonable, it was decided that a computational analogue be created. MCNP6 was chosen as the software to use in order to design this analogue. MCNP6 is a stochastic radiation transport code that offers several key advantages. First, the author of this thesis already had a working knowledge of the code from his background. Additionally, MCNP6 allows for user modification of the source code and redistribution of these changes through the use of patches. MCNP6 has a user base numbering in the tens of thousands and thus patches and third party tools developed in order to create the computational analogue can be used by others [5] [6]. MCNP6 has been used to model PSD's but only for efficiency and not position data [12]. Finally, a code such as GEANT4 may also be useful in terms of its ability to model position sensitive detectors as it has already been used in modeling the position response for gamma photon detectors [10]; however, the Texas A&M computational group is also developing a deterministic radiation transport code, Parallel Deterministic Transport (PDT). This code can interpret the geometry and material specifications from MCNP6 input files. Thus, for the sake of consistency, MCNP6 was selected as the modeling code.

2. CHARGED PARTICLE PHYSICS

Neutrons are not directly measurable by current radiation detection systems. Such systems rely upon the collection of electrons produced during an interaction in order to generate an electrical signal. However, neutrons do not directly ionize the medium they are traveling through. Thus, electron production must occur due to the production of secondary radiation due to a neutron interaction within the detection medium. If this secondary radiation is charged, then electron production will occur. While photons are neutral particles, they can directly ionize the detection medium through the photoelectric effect.

Neutral and charged particles differ in several important ways. If a charged particle with some initial energy is traveling through a medium, it will eventually lose all of its energy and come to a stop. The distance it travels in the medium is known as the stopping range (SR). On the other hand, neutral particles undergo what is known as exponential attenuation. If monoenergetic neutral particles travel through a detection medium, they all will not stop at the same distance. Rather, there will be a distribution of distances where the neutral particle is stopped.

There are also differences between the transport of electrons and heavy charged particles (HCP's). Electrons are much less massive than heavier charged particles, with a mass difference typically on the order of 10^{-4}. This results in electrons having curved trajectories while traveling through a medium. Each Columbic interaction can so strongly alter the trajectory of an electron such that they do not travel in straight lines.

On the other hand, HCP's traveling through a medium do (on average) travel in straight lines. While a few HCP's will be scattered off at some angle (the Rutherford gold foil experiment demonstrated this, thus showing the existence of the nucleus), almost all of them will end up traveling in a straight line as the Columbic interactions they undergo will change their momentum much less compared to the impulse received by electrons [8]. This result will be important for later and will be confirmed by using MCNP6 and the Stopping Range of Ions in Matter (SRIM) code in Section 4.

In general (for non-relativistic particles), the stopping power of a HCP can modeled as [8]:

$$\frac{dE}{d\vec{r}} = \frac{4\pi k_0^2 z^2 e^4 n}{mV^2} \ln\left(\frac{2mV^2}{I}\right). \tag{2.1}$$

Where E is the energy of the heavy charged particle, $\vec{r}$ is the position of the heavy charged particle, k_0 is Coulomb's constant, z is atomic number of the HCP, e is the charge of an electron, n is the number density of electrons in the medium, m is the mass of an electron, V is the velocity of the heavy charged particle, and I is the mean excitation energy. From Eq. (2.1) it becomes obvious that the stopping power is dependent on material properties as the function includes both the electron number density and the mean excitation energy. Eq. (2.1) can also be written with several correction terms for relativistic particles and corrections due to the HCP having electrons (shell corrections) which are incorporated into MCNP. However, for the purpose of this project, non-relativistic HCP's will be assumed and Eq. (2.1) is valid. Since the particles are non-relativistic, Eq. (2.1) can be further simplified:

$$\frac{dE}{d\vec{r}} = \frac{2\pi k_0^2 z^2 e^4 nM}{mE} \ln\left(\frac{4mE}{IM}\right). \tag{2.2}$$

With M as the mass of the HCP. The mean excitation energy for various elements can be determined from the following set of empirical relations [8]:

$$I = 19.0\ eV, Z = 1. \tag{2.3}$$

$$I = 11.2 + 11.7Z\ eV, 2 \leq Z \leq 13. \tag{2.4}$$

$$I = 52.8 + 8.71Z\ eV, Z > 13. \tag{2.5}$$

Assuming a compound material, the mean excitation energy can be computed by considering the various constituents of the material [8]:

$$n\ln I = \sum_{i=1}^{\infty} n_i z_i \ln I_i. \tag{2.6}$$

Additionally, the overall electron density can be computed from [8]:

$$n = \sum_{i=1}^{\infty} N_i z_i. \tag{2.7}$$

Where N is the atom density. Electrons are removed from the medium atoms due to the deposition of energy from the HCP into the medium. The process of electron removal simply requires an electron in an atom receiving enough energy beyond the threshold for ionization. Determining exactly how many electrons (and from which orbital shells) are removed due to energy is beyond the scope of this thesis as it involves several advanced quantum mechanical models. However, what can be understood is that assuming a large enough deposition of energy that there is some average number of electrons (from whichever shell) that are removed.

3. CURRENT TECHNOLOGY

Neutron detection technologies have been around for decades [1]. Some of the first neutron detectors were gas-filled cylinders. These detectors are still used for several reasons. Thermal neutrons have a high interaction probability with the gas while gamma photons have a much lower interaction probability [1]. This allows for these types of detectors to easily see thermal neutrons while receiving little amounts of noise from gamma photons. Additionally, these gas detectors are very cheap and thus a viable option over more expensive scintillation detectors.

These gas detectors work by choosing a gas that when undergoing a reaction with a neutron, allows for the production of HCP's. The PSD chosen for use by the CERT group is filled with BF_3 gas. The neutron directly interacts with the ^{10}B atom through the mechanisms given by Eqs. (3.1) and (3.2) [1]:

$$^{10}B + n \rightarrow {}^{7}Li^{*} + {}^{4}He + 2310 \text{ keV}. \tag{3.1}$$

$$^{7}Li^{*} \rightarrow {}^{7}Li + 480 \text{ keV}. \tag{3.2}$$

Eqs. (3.1) and (3.2) can be interpreted in order to determine the total energy deposition of the HCP's (and gamma photons) into the detector volume. After about 94% of these neutron interactions, the ^{7}Li ion is left in an excited state and subsequently releases a gamma photon which has a kinetic energy of 0.480 MeV. As stated before, BF_3 gas detectors have a low probability of having an interaction with this gamma photon and thus typically none of the energy from the gamma photon is deposited into the detector. On the other hand, 6% of the time the ^{7}Li ion is left in its ground state and no gamma

photon is released. When the ^{7}Li ion is left is an excited state and subsequently emits a gamma photon, the kinetic energies of the lithium ion and alpha particle are 1.02 MeV and 1.78 MeV respectively. When the ^{7}Li ion is left in its ground then the kinetic energies are then 0.84 MeV and 1.47 MeV. Thus, the total energy deposition can be either 2.31 MeV (94% probability) or 2.79 MeV (6% probability) assuming that the gamma photon leaks out of the detector without undergoing an interaction.

This total energy deposition however is only true if the detector volume is infinite. While, each of these HCP's (at these initial kinetic energies) only has a SR of several cm, that SR may be larger than the distance each particle travels before hitting the wall of the detector and exiting the detector volume through surface leakage. In this case, the total energy deposition from each neutron interaction is less than the theoretical maximum. This is known as the "wall effect". Why? Well for interactions located closest to the walls of the detectors the total energy deposition will be the smallest due to the increased likelihood of surface leakage of a HCP. Figure 3.1 shows that the total energy deposition for a dummy BF_3 does not always match the discrete values of either 2.31 MeV or 2.79 MeV. Additionally, Figure 3.1 shows that the 2.79 MeV total energy deposition probably is higher than the probability for the 2.31 MeV total energy deposition reaction. Finally, Figure 3.2 shows a physical representation of the HCP's traversing their SR's in the detection medium. From Figure 3.2 it is obvious to see that it is possible for the resultant particles to leak out of the detector before depositing all of their energy.

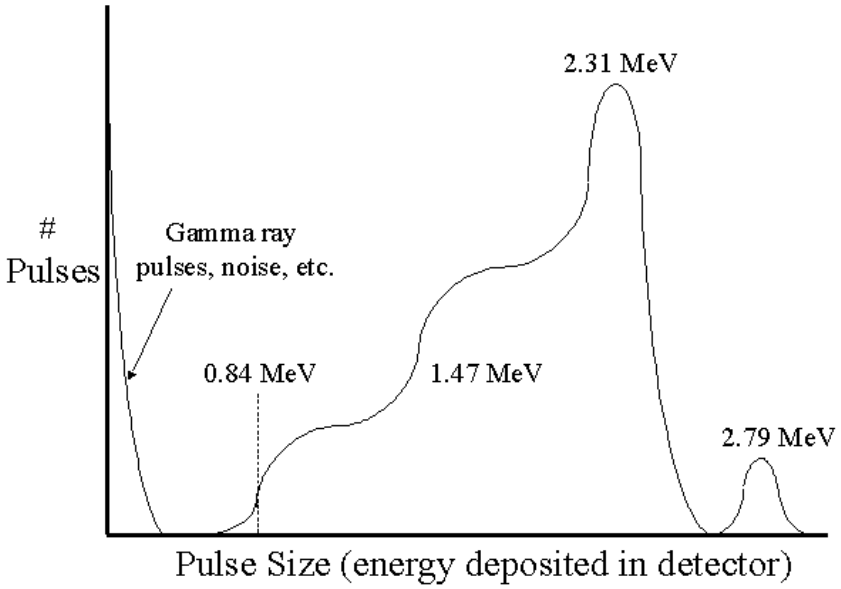

Figure 3.1: Sketch (not from an actual detector) neutron energy spectrum for a finite BF_3 detector. Reprinted from [9].

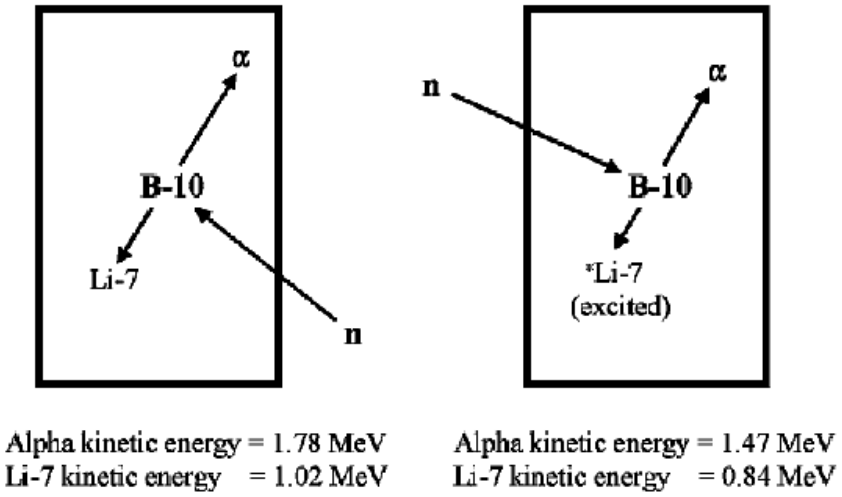

Figure 3.2: Physical representation of the resultant HCP's traveling through the BF_3 detection medium. Reprinted from [9].

While the predominant reaction is defined by Eqs. (3.1) and (3.2) there are also additional reactions which will be detected by the BF_3 which must be accounted for. Plots of the cross sections of these reactions are shown in Figures 3.3 and 3.4. The data shown in Figures 3.3 and 3.4 comes from the Evaluated Nuclear Data File (ENDF) accessed through the Nuclear Energy Agency's JANIS service [14].

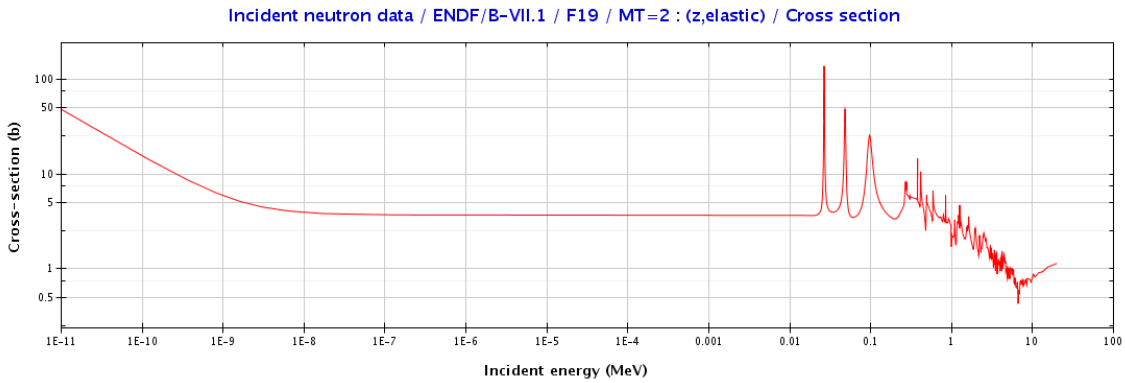

Figure 3.3: Neutron reaction cross sections for ^{19}F. Reprinted from [14].

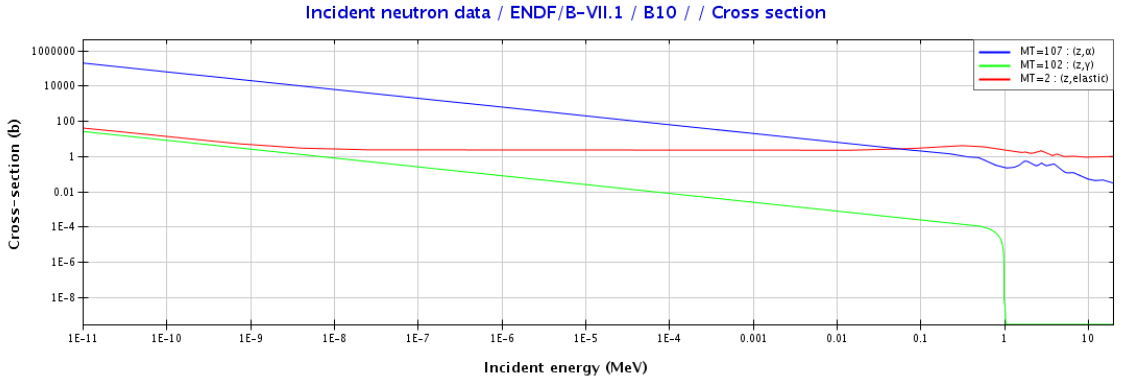

Figure 3.4: Neutron reaction cross sections for ^{10}B. Reprinted from [14].

From Figure 3.3 it is obvious that the predominant way for a neutron/^{19}F interaction to result in the production of electrons is the elastic scattering of ^{19}F which then subsequently produces a trail of electrons in the gas medium. Additionally, from

Figure 3.4 it is obvious that in addition to the reactions described by Eqs. (3.1) and (3.2) are not the only mechanisms from which electron production can occur due to a neutron/^{10}B reaction. It is also possible for the production of a gamma photon and a recoiling ^{10}B (of which only the ^{10}B will interact with the gas and produce electrons). Finally, another possibility is the production of ^{11}B which can create its own trail of electrons as it traverses the gas medium.

As discussed in Section 2, electrons are generated along the path of HCP that is emitted after the neutron interaction. However, there are still several steps which need to take place in order to provide an electrical signal to the detector. First, these electrons must be pulled towards the detector anode wire by an applied electric field described by Eq. (3.3) [2].

$$E(r) = \frac{V}{r\ln(\frac{b}{a})}. \tag{3.3}$$

Where E is defined as the electric field, V is the applied voltage, r is the radial distance from the anode wire, b is the cathode wire inner radius and a is the anode wire outer radius. The electric field is directly inwards radially from the anode wire. It is assumed that the initial electrons generated move along the electric field lines coming from the anode wire.

Gas detectors operate in what is known as the “proportional region”. This means that the applied voltage is high enough so that when the electrons are being pulled towards the anode wire, once they are close enough to the anode wire then they will ionize additional gas molecules. This is due to the electrons being accelerated to a high

enough velocity such that they knock loose additional electrons. The resultant electron-ion pairs move towards the anode wire and knock loose additional electrons. This cascading process (known as the Townsend avalanche) continues until all electrons which results from the initial electron are collected on the anode wire. Thus, a multiplication process has occurred. The total number of electrons collected on the anode wire resultant from one neutron interaction is a multiplicative factor higher than the number of electrons initially generated [2]. This allows for a clear electrical signal to be generated by the detectors and read by the circuits.

3.1 Position Sensitive Detectors

The type of detector described in Section 3 only gives information on the presence of a neutron. Total neutron counting is a useful tool in that simply determining the presence of neutrons by seeing if an electrical pulse is generated. Simply detecting the presence of neutrons is important in areas of non-proliferation. However, this project seeks to determine not only the presence of thermal neutrons within the detector region but also the location of their interaction. Thus, modifications to the circuits attached to the detectors discussed in Section 3 will now be discussed here.

The development of PSD's began shortly after the general development of thermal neutron detectors. These detectors can report the position of the neutron interaction using either a single or multiple anode wires depending on if position information for a single or for multiple dimensions is desired. The basic principles of these detectors have remained unchanged since the 1960's. While there has been some development in terms of the accuracy of these detectors, an error analysis of the

experiment results will be the concern of the experimentalists [3] [4]. Additionally, this study will only look at 1D detectors as that is the detector currently being used at the Nuclear Science Center.

The basic principle of getting information about the position of the neutron interaction is determining the location of the charge centroid correspond to the collection of electrons on the anode wire. Eq. (3.4) shows how to compute the charge centroid for a BF_3 detector which only has two products which produce electrons:

$$\overrightarrow{r_Q} = \frac{\int q_\alpha(\vec{r})\vec{r}d\vec{r} + \int q_{Li}(\vec{r})\vec{r}d\vec{r}}{Q_\alpha + Q_{Li}}. \tag{3.4}$$

Where $\overrightarrow{r_Q}$ is the position of the charge centroid, $q_\alpha(\vec{r})$ is the charge per unit length produced along the path of the alpha particle, $q_{Li}(\vec{r})$ is the charge per unit length produced along the path of the ^{7}Li, Q_α is the total charge produced by the alpha particle, and Q_{Li} is the total charge produced by the ^{7}Li ion. The location of this charge centroid is then projected unto the anode wire. Assuming that the anode wire is straight (a pre-requisite for Eq. (3.3)) then this projection becomes:

$$\overrightarrow{r_x} = \frac{\overrightarrow{r_Q} \cdot \overrightarrow{r_a}}{|\overrightarrow{r_a}|^2}\overrightarrow{r_a}. \tag{3.5}$$

With $\overrightarrow{r_x}$ as the projection of the charge centroid unto the anode wire and $\overrightarrow{r_a}$ as the vector going from the start to the end of the anode wire. A 1D thermal neutron detector obviously only gives a single value for the position of the neutron interaction:

$$x = |\overrightarrow{r_x}|. \tag{3.6}$$

Where x is the position readout from the detector. There are two main methods for determining this position value: charge division and time delay methods.

The charge division method relies upon the anode wire having a constant per unit length resistance. Given that the electrical resistance0 is for a linear resistive unit is directly proportional to its length and by exploiting Kirchoff's Laws, the position value given using the charge splitting method is given by [2] [11]:

$$x = \frac{Q_1}{Q_1 + Q_2} L. \tag{3.7}$$

With Q_1 as the total charge collected on the "left" end of the anode wire, Q_2 as the total charge collected on the "right" end of the anode wire, and L as the total length of the anode wire. Figure 3.5 shows an example of a 1D PSD for gamma photons.

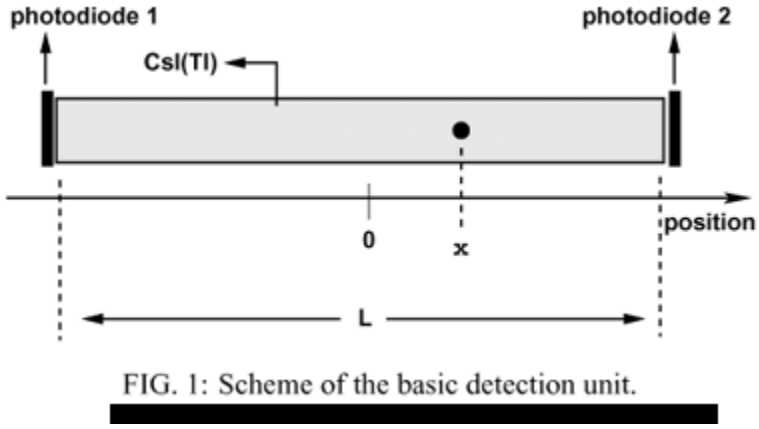

Figure 3.5: Schematic for a gamma photon PSD. Reprinted from [10].

The main difference between Figure 3.5 and the equations being derived here is that in Figure 3.5 the origin is placed at the axial center of the detector while for the equations in this thesis the origin is placed at the "left" end of the detector. And obviously neutron detectors are being examined instead of gamma ray detectors.

Eq. (3.7) can be derived by assuming that the total electron collection onto the anode wire can be modeled as having all the electrons hitting the anode wire at a single

point. Thus, the cascade of electrons can be modeled as a current. Thus, the anode wire can be modeled as a current dividing circuit. Given that the electrical resistance is:

$$R = \rho \frac{l}{A}. \tag{3.8}$$

where ρ is the material resistivity, l is the resistive element length, and A is the resistive element cross section area (geometric). The resistance of the left and right sections of the anode wire relative to x can now be computed as:

$$R_1 = \rho \frac{x}{A}. \tag{3.9}$$

$$R_2 = \rho \frac{L - x}{A}. \tag{3.10}$$

The current-division nature of the circuit also allow for additional equations:

$$Q = Q_1 + Q_2. \tag{3.11}$$

$$Q_1 = \frac{R_2}{R_1 + R_2} Q. \tag{3.12}$$

$$Q_2 = \frac{R_1}{R_1 + R_2} Q. \tag{3.13}$$

where Q is the total charge collected. Following algebraic manipulation, Eqs. (3.9) through (3.13) can be used to show the validity of Eq. (3.7).

The time delay method relies upon the anode wire having both a per unit length resistance and a per unit length capacitance (an RC transmission wire). By once again exploiting Kirchoff's laws, the position of the charge centroid projected onto the anode wire can be found to be [11]:

$$x = \frac{L}{2}\left[\frac{(t_1 - t_2)}{RC} + 1\right]. \tag{3.14}$$

Where L is the total length of the anode wire, t_1 is rise the time for the charge to build up on the "left" side of the detector, t_2 is the rise time for the charge to build up on the "right" side of the detector, R is the total electrical resistance of the anode wire, and C is the total capacitance of the anode wire. Eq. (3.14) can be derived by first writing down the resistances and capacitances of each side of the anode wire:

$$R_1 = \frac{x}{L}R. \tag{3.15}$$

$$R_2 = \frac{L - x}{L}R. \tag{3.16}$$

$$C_1 = \frac{x}{L}C. \tag{3.17}$$

$$C_2 = \frac{L - x}{L}C. \tag{3.18}$$

Additionally, given that each segment of the anode wire is an RC circuit, the rise time for the charge to build up can be given by:

$$t_1 = R_1C_1. \tag{3.19}$$

$$t_2 = R_2C_2. \tag{3.20}$$

And thus from Eqs. (3.15) through (3.20) Eq. (3.14) can be found easily through algebraic manipulation.

Both of the primary methods of getting a reading on the location of the neutron interaction rely on determining the location of the charge centroid collected on the anode wire. Because there is only a single anode wire, only a single position value can be given. So there may be neutron interactions which occur at different locations but who

charge centroid gives the same projection unto the anode wire due to having the charge generation centroid at the same axial position. While MCNP6 can determine the location of this charge centroid in all three dimensions, the code development will only provide a single position value along the anode wire to be the output.

3.2 MCNP6: Stochastic Radiation Transport

MCNP6 is considered the gold standard for stochastic radiation transport codes. The code works by the user defining 1) the problem geometry 2) the materials present in each part of the problem geometry 3) the source definition and 4) physics and statistics models to be used for the simulation. The user selects a certain number of particles to be run. MCNP6 will then simulate each of these particles as they traverse the problem geometry until some condition is met such as the particle reaching a low enough energy or the particle exiting the problem geometry. MCNP6 also simulates each of the secondary radiation which are emitted due to an interaction between the source particle and the materials present in each section of the problem geometry. The initial properties of each source and secondary particle are determining through sampling procedures which make use of random number generators. The interactions each of these particles undergoes while traversing the problem geometry are also determined through the use of sampling procedures.

As an example, if a monoenergetic point isotropic source is selected as the source definition, then for each source particle that is transported MCNP will not sample from an energy distribution but will sample uniformly from the possible distribution of polar and azimuthal angles in order to determine the initial direction of the source particles

Because only one particle is run at a time, it is necessary to simulate many particles so that the source actually behaves like a point isotropic source.

MCNP6 contains several specific physics models relating to BF_3 detectors and the transport of the product HCP's which result from the neutron interaction which need to be discussed. First, there is only individual tracking for four specific types of heavy ions (which includes the alpha particle). All of the other species of heavy ions (including ^{7}Li) are tracked together as a group. Thus, some knowledge of the possible reactions which can occur within the BF_3 gas is necessary (for this project it was assumed that all resultant grouped heavy ions were either ^{7}Li, ^{10}B, ^{11}B, or ^{19}F). Additionally, MCNP6 does not actually track the generation of electrons along the path of the heavy charged particles. Therefore, the $q_{\alpha}(\vec{r})$ and $q_{Li}(\vec{r})$ terms in Eq. (3.4) cannot be directly computed. Therefore, in order to determine the charge centroid in MCNP6 several assumptions must be made. The material in the detector must be assumed to be homogeneous and that the HCP's cause enough ionization such that on average the number of electrons knocked loose per amount of energy deposited is constant. This allows for the simplifying assumption to be made:

$$q_{\alpha} = k\frac{dE_{\alpha}}{d\vec{r}}. \tag{3.21}$$

$$q_{Li} = k\frac{dE_{Li}}{d\vec{r}}. \tag{3.22}$$

Where k is a constant of proportionality defined by the medium the heavy charged particles are traversing through, E_α is the energy of the alpha particle and E_{Li} is the energy of the ^{7}Li ion. The total charge terms in Eq. (3.4) can then be re-written as:

$$Q_\alpha = k \int \frac{dE_\alpha}{d\vec{r}} d\vec{r}. \tag{3.23}$$

$$Q_{Li} = k \int \frac{dE_{Li}}{d\vec{r}} d\vec{r}. \tag{3.24}$$

Finally, Eq. (3.4) can be re-written as:

$$\overrightarrow{r_Q} = \frac{\int \frac{dE_\alpha}{d\vec{r}} \vec{r} d\vec{r} + \int \frac{dE_{Li}}{d\vec{r}} \vec{r} d\vec{r}}{(E_{\alpha,f} - E_{\alpha,0}) + (E_{Li,f} - E_{Li,0})}. \tag{3.25}$$

Where $E_{\alpha,f}$ and $E_{\alpha,0}$ are the final and initial energies of the alpha particle and $E_{Li,f}$ and $E_{Li,0}$ are the final and initial energies of the lithium ion. MCNP6 does offer ways to track the energies of the alpha particles and ^{7}Li ions; therefore, Eq. (3.25) can be used in conjunction with Eq. (3.5) in order to determine the predicted position reading.

MCNP6 also has one noticeable deficiency in its physics models in terms of modeling the resultant products in Eqs. (3.1) and (3.2). The gamma photon in Eq. (3.2) does not instantaneously decay. Instead the^{7}Li ion will remain in an excited state for a short time. However, MCNP6 models the ^{7}Li ion as having already ejected the gamma photon and being at 0.84 MeV. This is not technically correct, although the ^{7}Li ion may decay so quickly that it does not really matter.

Additionally, MCNP6 does not have options for simulating electric fields. Therefore, the electric field generated by the anode wire and described by Eq. (3.3) cannot be inserted into the problem geometry. A code such as GEANT4 would be able

to simulate this electric field. In order to get around this, it is assumed that each generated electron only starts an avalanche at a specific distance from the anode wire. Thus, the centroid of the charge generation remains the centroid of the charge collection on the anode wire [2] [5].

Finally, it should be noted that Eq. (3.25) can be re-written to consider the other possible neutron reactions in the BF_3. It is as simple as only including the terms for energy deposition due to the scattered ^{10}B, ^{11}B, or ^{19}F.

4. METHODOLOGY

MCNP6 can compute “tallies” or calculations of various parameters. For example, MCNP6 can compute the total energy deposition for a given type(s) of particle(s) in a given cell. This value is then normalized by the mass of the cell (given the cell’s volume and mass density) and by also normalized by the number of source particles chosen to be run. The “tally” given from each calculation (as MCNP6 is a stochastic code) is obviously more accurate given a larger number of source particles (and therefore greater computational expense).

Vanilla MCNP6 allows for the user to compute a type of calculation which predicts the response for a position sensitive detector. The position sensitive detector can be treated by modeling the detector gas volume as multiple cells rather than a single cell. Next, MCNP6 can compute a F6 energy deposition tally for each of these cells which compose the position sensitive detector. In the resultant MCNP6 output file, energy deposition normalized by the mass and number of source particles in each sub-cell of the position sensitive detector will be given. There are several problems with this method. First, this method does not track individual neutron interactions, only the total energy deposition due to secondary radiation resultant of all neutron interactions. Secondly, this method can be computationally expensive as if a very fine spatial resolution is desired.

Therefore, two main methods will be proposed in order to determine the position value reported by the detector and also the actual position of the neutron interaction. The first method will involve exploiting the MCNP6 PTRAC utility. The PTRAC utility

allows the user to export a list of particle events (generated from a list of conditions) to an output file. This PTRAC utility will be used to show that the resultant products from in Eqs. (3.1) and (3.2) lose energy at a constant rate with respect to their displacement in the gas volume. This will allow for a simplification to Eq. (3.25) and thus PTRAC will be used in order to determine both the detector response as well as the actual location of the neutron interaction.

Additionally, MCNP6 has a user-defined subroutine called TALLYX. Once this sub-routine is written and the source code is recompiled, modifications to the default tallies are allowed. At each sub-step of the default tally calculation, TALLYX will also be called [5]. This allows for TALLYX to use the information at the current sub-step in order to compute some new value.

4.1 PTRAC

The MCNP PTRAC utility allows for user-selected events to be sent to an output file. PTRAC will now be used in order to show that energy loss is constant with respect to displacement for an alpha particle and a ^{7}Li ion with starting energies as shown in Figure 3.2. An MCNP input file was arranged such that source was either a 1.78 MeV or 1.47 MeV alpha particle moving upwards in the positive Z-direction through a homogeneous BF_3 gas of density 0.00074755 g cm^{-3} and thickness 10 cm with cell divisions at every 0.0001 cm in the Z-direction. A total of 10 source particles were run. The PTRAC files allows for the user to output 1) surface crossing events and 2) termination events. PTRAC can also list the particle type, position, direction cosines, energy, time, and particle importance for each event. Thus, this output file can be used in

order to extract an $E(\vec{r})$ within a specific gas medium for each of the alpha particle and ^{7}Li ion. Figure 4.1 shows an example of a PTRAC file.

Figure 4.1: Example PTRAC file with designated particle events separated into blocks by source particle number. Reprinted from [7].

From Figure 4.1 it is obvious that PTRAC files are written in such a way that large amounts of information are present and particle event information is separated by the source particle corresponding to those particle events. Thus, it should be feasible to write data processing utilities which can read PTRAC files determine events occurring due to individual neutron interactions. Figure 4.2 and Figure 4.3 show a reconstruction of $E(\vec{r})$ based upon surface crossing information from the described simulation.

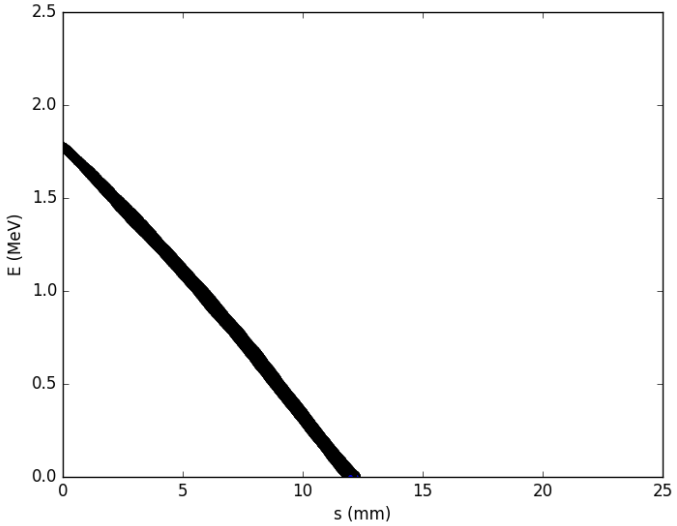

Figure 4.2: Energy of a 1.78 MeV alpha particle traversing BF_3.

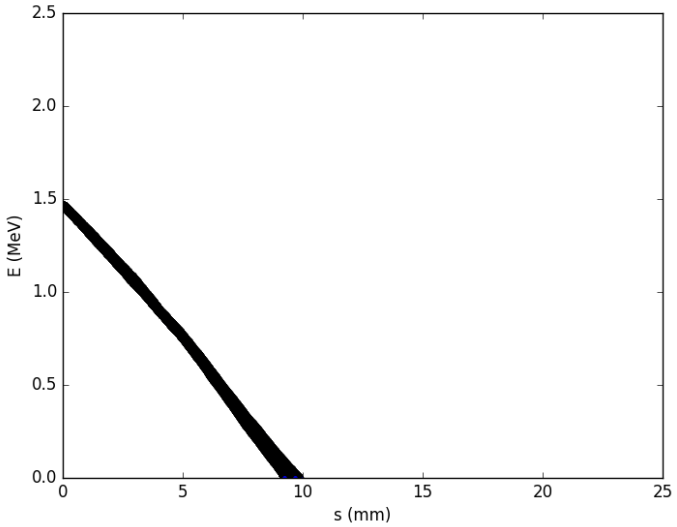

Figure 4.3: Energy of a 1.47 MeV alpha particle traversing BF_3.

From Figure 4.2 and Figure 4.3 it is obvious that $E(\vec{r})$ is linear over the entire path of the particle. A regression analysis assuming that E is linear with respect to $\vec{r}$ gave $R^2 = 0.997262399335$ for the case in Figure 4.2 and $R^2 = 0.998362384677$ for the case

in Figure 4.3. This is highly linear relation. Additionally, from Figure 4.2 the stopping range of the 1.78 MeV alpha particle in this BF_3 gas is about 12 mm while for the 1.47 MeV alpha particle the stopping range is reduced to 10 mm.

Additionally, a 1.02 MeV or 0.84 MeV ^{7}Li ion also traversed the same BF_3 gas with a thickness of 2.5 cm and a vertical discretization of 0.00005 cm. The $E(\vec{r})$ results from its surface crossings are shown in Figure 4.4 and Figure 4.5.

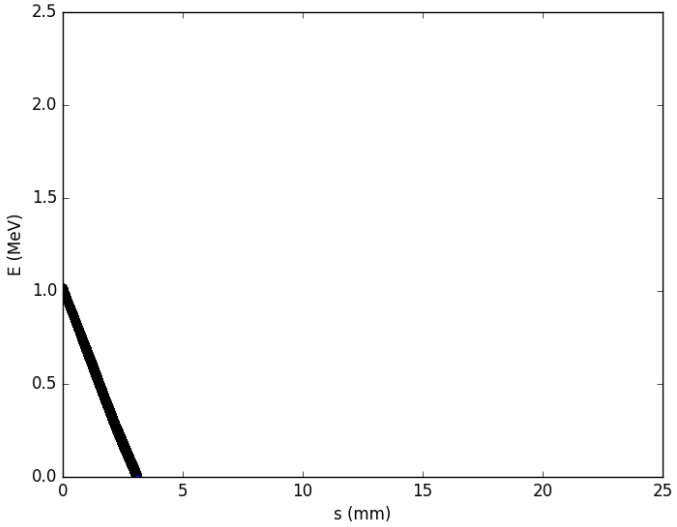

Figure 4.4: Energy of a 1.02 MeV lithium ion traversing BF_3.

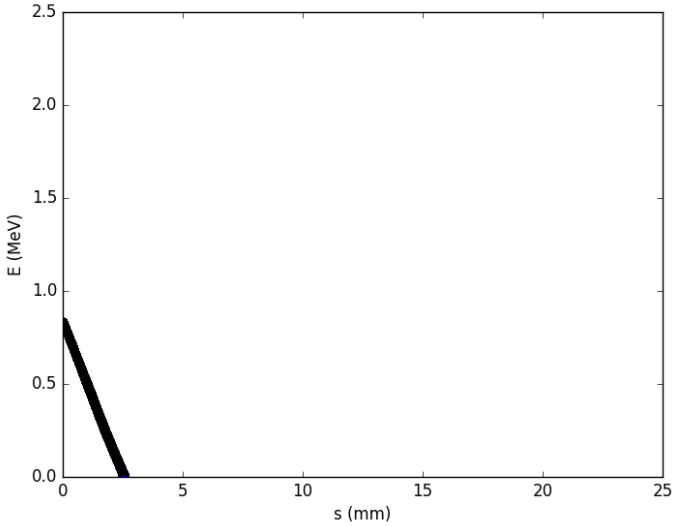

Figure 4.5: Energy of a 0.84 MeV lithium ion traversing BF_3.

From Figure 4.4 and Figure 4.5 it is obvious that $E(\vec{r})$ is linear for these starting energies of a ^7Li ion in BF_3. Specifically, a regression analysis assuming that E is linear with respect to $\vec{r}$ gave $R^2 = 0.999013226294$ for Figure 4.4 and $R^2 = 0.999094224011$ for Figure 4.5. This again represents a highly linear relation for $E(\vec{r})$ for these particular energies and medium for ^7Li. Finally, from Figure 4.4 the stopping range of the 1.02 MeV ^7Li ion is close to 3 mm while from Figure 4.5 the stopping range of the 0.84 MeV ^7Li ion is closer to 2.5 mm.

It should also be noted that the PTRAC file contains the X and Y position data at each surface crossing. This data indicates (after the PTRAC files were investigated) that for each of the HCP's that there was limited movement in the X and Y directions compared to the total displacement in the Z-direction. This is in agreement with the well-understood physics of HCP's traveling in straight lines (outside of massive deflections due to Rutherford scattering). Finally, it should be noted that the strong linearity in $E(\vec{r})$

may actually be unusual since typically there is a strong increase in $\frac{dE}{d\vec{r}}$ right before a charged particle loses all of its energy (Bragg peak) [8].

To further test the assumptions of the physics model, the same set-up was arranged and test using the Stopping Range of Ions in Matter (SRIM) code. This code performs a "Ion Distribution and Quick Calculation of Damage" computation as the HCP traverses the BF_3 in order to determine the SR of the particle within the medium. Note that SRIM considers the boron in the BF_3 to be B^{11}. Figure 4.6 shows 10,000 1.78 MeV alpha particles traveling through BF_3, Figure 4.7 shows 10,000 1.47 MeV alpha particles traveling through BF_3, Figure 4.8 shows 10,000 1.02 MeV ^{7}Li ions traveling through BF_3, and finally Figure 4.9 shows 10,000 0.84 MeV ^{7}Li ions traveling through BF_3.

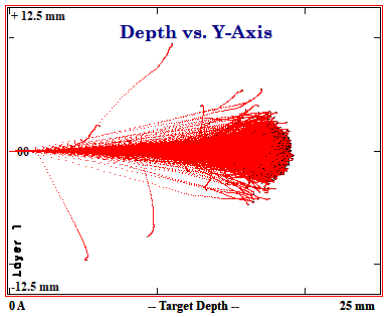

Figure 4.6: Ion damage results with SRIM for 1.78 MeV alpha particles in BF_3. Longitudinal range is 18.0 mm.

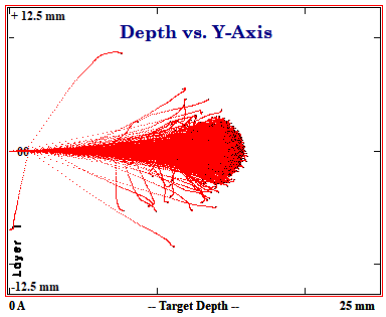

Figure 4.7: Ion damage results with SRIM for 1.47 MeV alpha particles in BF_3. Longitudinal range is 14.9 mm.

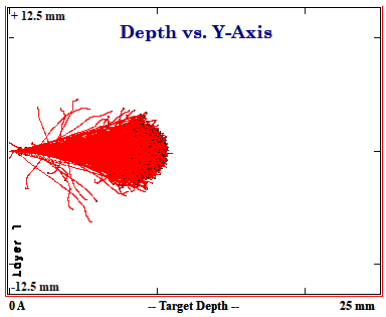

Figure 4.8: Ion damage results with SRIM for 1.02 MeV ^7Li ions in BF_3. Longitudinal range is 9.49 mm.

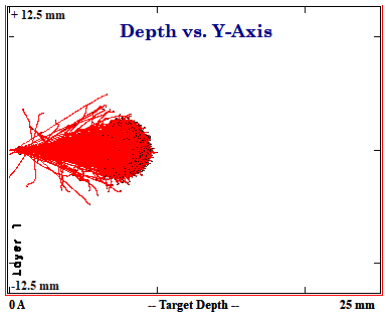

Figure 4.9: Ion damage results with SRIM for 0.84 MeV ^7Li ions in BF_3. Longitudinal range is 8.44 mm.

Comparing Figure 4.2 to Figure 4.6, Figure 4.3 to Figure 4.5, Figure 4.4 to Figure 4.8, and Figure 4.5 to Figure 4.9 it becomes obviously that there is a large

discrepancy in the results for the two calculations. MCNP gives a SR for a 1.78 MeV alpha particle, a 1.47 MeV particle, a 1.02 MeV ^{7}Li ion, and 0.84 MeV ^{7}Li ion respectively as approximately 12 mm, 9.5 mm, 3 mm, or 2.5 mm respectively. The SRIM SR results for these respective energies are 18.0 mm. 14.9 mm, 9.49 mm, and 8.44 mm. SRIM predicts for both alpha particles and ^{7}Li ions a much longer stopping range in the same material given the same initial energy. This could have to do with the different physics models for lower energy heavy charged particles. At lower energies, the effect of the electrons of the charged particle becomes more dominant. However, both SRIM and MCNP6 do predict that the particles generally travel in a straight line. For the SRIM results there are a handful of large deflections (again see the Rutherford gold foil experiment) but the particles mostly travel directly to the right with only a small amount of lateral displacement. Despite the discrepancy in the results, none of the SRIM numerical results will be used in this analysis as this is an MCNP6 project. However, this does call into question the integrity of position results obtained using MCNP6. How MCNP6 transports electrons is heavily documented [5]; however, transport is for HCP's is not, leading to the suspicion that perhaps the physics models for HCP's are not very robust.

As a final sanity check on the results in Figure 4.2 through Figure 4.9, a direct computation of the stopping range using the non-relativistic Bethe formula (Eq. (2.2)) and integrating over all possible energies. Eqs. (2.3) through (2.7). First, the mean excitation energy of boron is 69.7 eV and the mean excitation energy of fluorine is 116.5 eV. The electron density of the boron is $3.360 \cdot 10^{19}$ cm^{-3} and the electron density of the

fluorine is $1.814 \cdot 10^{20}$ cm^{-3}. Thus, the total electron density of the BF_3 gas is $2.150 \cdot 10^{20}$ cm^{-3}. Further, the mean excitation energy of the BF_3 gas is 107.5 eV (0.1075 MeV). Given that the mass of an electron is $5.488 \cdot 10^{-4}$ amu, the mass of an alpha particle is 4.003 amu, and the mass of a ^{7}Li ion is 7.016 amu, a relation for the SR of the transported ions can be determined for both alpha particles (Eq. (4.1)) and ^{7}LI ions (Eq. (4.2)):

$$\mathrm{SR} = \int \frac{\mathrm{EdE}}{8.175 \cdot 10^{10} \ln(5.101 \cdot 10^{-6} \mathrm{E})}. \tag{4.1}$$

$$\mathrm{SR} = \int \frac{\mathrm{EdE}}{3.224 \cdot 10^{11} \ln(2.911 \cdot 10^{-6} \mathrm{E})}. \tag{4.2}$$

Where the units of energy are in eV and the units for stopping range are in mm. Thus, the stopping range can be computing by integrating Eqs. (4.1) and (4.2) from the starting particle energy down to the cutoff energy of 1000 eV. Eq. (4.1) gives the SR of a 1.78 MeV alpha particle to be 12.33 mm and the SR of a 1.47 MeV alpha particle to be particle to be 10.40 mm. Additionally, Eq. (4.2) gives the SR of a 1.02 MeV ^{7}Li ion to be 2.063 mm and the SR of a 0.84 MeV ^{7}Li ion to be 1.541 mm. These calculations show much more congruency with the MCNP6 than the SRIM results. This could be due to the SRIM calculation not being selected to be detailed enough or due to different physics models used in MCNP6 vs. SRIM calculations. In any case, due to these various differences in results there is reason to believe that either the MCNP6 models are incomplete or that during MCNP6 simulations additional physics models needed to be added to the input file. Table 4.1 summarizes these various results.

Table 4.1: SR as predicted from each of the three methods.

	SRIM (mm)	Approximate MCNP (mm)	Bethe (mm)
Alpha, 1.78 MeV	18	12	12.33
Alpha, 1.47 MeV	14.9	9.5	10.4
Lithium, 1.02 MeV	9.49	3	2.063
Lithium, 0.84 MeV	8.44	2.5	1.541

One final explanation for the discrepancies between these results is that fluorine chemical bonding (as take place in BF_3) causes large shifts in I. However, SRIM does not have BF_3 available as a material with corrections to the mean excitation energy due to chemical bonding. Instead, the SRIM simulations were performed assuming that the BF_3 fit into a standard compound model. However this is not the case due to fluorine chemical bonding [15].

Now that the linearity between the energy and displacement for both ^{7}Li ions and alpha particles in BF_3 gas has been established, Eq (3.25) can be greatly simplified. Eq. (3.25) can now be re-written. The energy of each of the alpha particle and 7Li ion can first be written as:

$$E_\alpha = E_{s,\alpha} + \frac{E_{t,\alpha} - E_{s,\alpha}}{|\overrightarrow{r_{t,\alpha}} - \overrightarrow{r_{s,\alpha}}|} |\overrightarrow{r_\alpha} - \overrightarrow{r_{s,\alpha}}|. \tag{4.3}$$

$$E_{Li} = E_{s,Li} + \frac{E_{t,Li} - E_{s,Li}}{|\overrightarrow{r_{t,Li}} - \overrightarrow{r_{s,Li}}|}|\overrightarrow{r_{Li}} - \overrightarrow{r_{s,Li}}|. \tag{4.4}$$

Where E_{α} is the energy of the alpha particle, $E_{s,\alpha}$ is the initial energy of the alpha particle, $E_{t,\alpha}$ is the termination energy of the alpha particle, $\overrightarrow{r_{\alpha}}$ is the position of the alpha particle, $\overrightarrow{r_{t,\alpha}}$ is the final position of the alpha particle, and $\overrightarrow{r_{s,\alpha}}$ is the initial position of the alpha particle. Additionally, E_{Li} is the energy of the ^{7}Li ion, $E_{s,Li}$ is the initial energy of the^{7}Li ion, $E_{t,Li}$ is the termination energy of the ^{7}Li ion, $\overrightarrow{r_{Li}}$ is the position of the ^{7}Li ion, $\overrightarrow{r_{t,Li}}$ is the final position of the lithium ion, and $\overrightarrow{r_{s,Li}}$ is the initial position of the lithium ion. Thus, Eq. (3.12) can be re-written as:

$$\overrightarrow{r_{Q}} = \frac{(E_{s,\alpha} - E_{t,\alpha})(\overrightarrow{r_{t,\alpha}} + \overrightarrow{r_{s,\alpha}}) + (E_{s,Li} - E_{t,Li})(\overrightarrow{r_{t,Li}} + \overrightarrow{r_{s,Li}})}{2[(E_{s,\alpha} - E_{t,\alpha}) + (E_{s,Li} - E_{t,Li})]}. \tag{4.5}$$

Eq. (4.5) can only be used by appropriately setting up the MCNP6 input file. First, Eq. (4.5) assumes that the only HCP's which are generated within the detector gas volume come from neutron interactions within the gas. While this will be mostly true it is not impossible for secondary radiation to penetrate the detector wall from the outside and deposit energy into the detector volume. However, this is not typically what happens and therefore the simplification can be made that the only HCP's that are of concern come from interactions within the detector gas volume. This simplification is also important as by not simulating the production or transport of HCP's in other parts of the problem geometry, computational expense is greatly lowered. Additionally, Eq. (4.5) assumes that a neutron interaction necessarily results in the production of an alpha particle and ^{7}Li ion every time. However, this is not true-as stated before elastic

scattering events can occur in which case only the term for the heavy ion (^{7}Li, ^{10}B, ^{11}B, or ^{19}F) will be taken into account. Finally, reading from the PTRAC file can give both the results of the detector response as well as the actual location of the neutron interaction. Having both of these results allows for a comparison of the neutron distribution in order to observe a wall effect.

In order to properly generate the PTRAC file, several steps must be taken. First, the user must define an F6 (total energy deposition) tally for the gas volume cell which includes both alpha particles and generic heavy ions. Next, the user must ask for all the PTRAC output to be all particle events which contribute to the F6 tally. Thus, the PTRAC file will include both birth and termination events for all product heavy ions and alpha particles. An alternate way to perform would be to not specify a tally with PTRAC and instead directly call for birth and termination events of alpha particles and heavy ions. Because alpha particles and heavy ions are killed once leaving the gas volume, termination events correspond to both surface leakage of HCP's as well termination due to the particle energy being too low.

PTRAC files are difficult to interpret from their explanation given in the MCNP6 user manual. A simpler explanation follows. Each block within the PTRAC output file represents all the particle events which correspond to a source particle. The number of the source particle is given in each block. Additionally, for each particle the type of event (looking for birth or termination), type of particle, and particle position, direction, energy, weight, and time are given. All of this information allows for a computation of the electron generation centroid.

The type of reaction which occurs is determined from the particle weight. To greater simply matters, MCNP6 treats each generated particle differently. Effectively each particle that is transported in MCNP6 is only actually some fraction (weight) of a particle. HCP's have a constant weight as they traverse a medium. Thus, all particle events within a source particle data block where the weight is the same correspond to a single reaction, either an alpha particle-^{7}Li ion pair or an elastic scatter. Thus, when the position projection from Eqs. (3.5) and (3.6) for either the neutron interaction or detector response is calculated the value entered into the histogram bin is the weight for the particles in the reaction. This is the correct way of performing this calculation as MCNP6 performs a similar method when computing surface fluxes [5].

4.2 TALLYX

MCNP6 contains a blank subroutine file (TALLYX) which the user is allowed to modify in order to compute custom tallies. The custom tallies are based upon the default tallies. If some tally Fn is asked to be calculated then this tally can be modified with the FUn tally. TALLYX is only called if FUn is present in the MCNP6 input file. TALLYX is written in FORTRAN90 and after the subroutine is written the entire MCNP6 executable must be re-compiled. The author of this thesis compiled the new build on Ubuntu 16.04 using the gfortran 5.4 and gcc 5.4 compilers [5] [6].

TALLYX is called for each substep of the tally computation. If a tally considers certain types of particles then each substep contains information on the particle type, position, and energy. Therefore, it is obvious how TALLYX can be used in order to

determine position information as information on particle energy and position as each particle in a tally traverses a cell is available.

The main method is to insert a F6:A,# energy deposition calculation into the input file. This method will be largely similar to the PTRAC method discussed in Section 4.1. Essentially, each time TALLYX is called information about the current substep of the calculation (particle type, position, energy, current source particle count) is written to an output file. In a way, this is similar to how a PTRAC file can contain information regarding these same properties but only for the birth and termination points for each particle. However, this method should provide the largest accuracy because as seen in Section 4.1 and Figures 4.5 through 4.9 that assuming that these HCP's travel in entirely straight lines is not entirely appropriate. And even if the paths are on average straight, the distance traveled is greater than a direct path from starting point to end point. Additionally, linearity was not established for the additional elastic scatter reactions or for alternate materials or gas densities. While the written output file does not contain all information regarding the path of each heavy charged particle, the discretization is very fine-some of the test problems showed that about 10^4-10^5 events were written while tracing each HCP. Thus, a modified form of Eq. (4.5) is required in order to properly mine this new PTRAC-like file:

$$\overrightarrow{r_Q} = \frac{\sum_{n=1}^{\infty}\left[\left(E_{s,\alpha} - E_{t,\alpha}\right)\left(\overrightarrow{r_{t,\alpha}} + \overrightarrow{r_{s,\alpha}}\right)\right]_n + \sum_{m=1}^{\infty}\left[\left(E_{s,Li} - E_{t,Li}\right)\left(\overrightarrow{r_{t,Li}} + \overrightarrow{r_{s,Li}}\right)\right]_m}{\sum_{n=1}^{\infty}\left[2\left(E_{s,\alpha} - E_{t,\alpha}\right)\right]_n + \sum_{m=1}^{\infty}\left[2\left(E_{s,Li} - E_{t,Li}\right)\right]_m}. \quad (4.6)$$

Eq. (4.6) is nearly similar to Eq. (4.5) with one noticeable difference. Instead of assuming constant energy loss over the entirely length of the particle trajectory, instead

energy loss is assumed to be constant (constant stopping power) between each of the many substeps for each particle. The subscripts “n” and “m” refer to the substeps of the alpha particle and ^{7}Li ion respectively. Obviously, as with previous methods discussed Eq. (4.6) can also be used just in the case of the solo production of a HCP from elastic scatter. Similar to the PTRAC method, the output file is mined for the necessary information. For each source particle, all energy deposition from HCP’s traversing the cell is considered. A position is then calculated and binned using Eq. (3.5).

This method holds the most promise and follows the greatest rigor. However, one severe limitation is that the output files generated can be quite large (in excess of 1 GB). While there may be a limitation in terms of disc space, Python is perfectly capable of reading these large files in a matter of 5-10 minutes per 1 GB of text file data. Still, a way to store this data in memory would be useful for rigor and also preventing overfilling the local drive. A likely method would be to avoid writing this large file to begin with and create additional global variables within the MCNP6 source code. However, this was found to require extensively modifying the MCNP6 source code. Such an undertaking would be beyond the scope of this project and it would reduce the ability for other users to implement the methods developed in this project.

5. TEST PROBLEMS AND RESULTS

There were three problems analyzed by running an MCNP6 simulation for them and then subsequently analyzed using each of the three methods discussed in Section 4. The problems were analyzed first by plotting the total counts in each position bin (which corresponds to an multi-channel analyzer channel) as computed from each method along with error bars. Because counts are being recorded, Poisson statistics can be used and the error in measure of counts is

$$\sigma_N = \sqrt{N}. \tag{5.1}$$

Where σ_N is the error in total counts and N is the total numbers of counts recorded in each MCA channel.

Next, a direct comparison of the PTRAC neutron collision location and PTRAC detector response methods will be performed. A comparison with the TALLYX substeps method can not be performed because TALLYX and PTRAC do not necessarily record information for same number of events. PTRAC collision and detector response methods always directly compare the same events. By propagating errors, the error in the difference of counts can be determined to be

$$\sigma_{N,\text{collision}-N,\text{response}} = \sqrt{N_{\text{collision}} + N_{\text{response}}}. \tag{5.2}$$

Without the presence of the wall effect (or energy spreading in general), it would be assumed that there is no difference in the total number of counts in each of the bins using

either the PTRAC collision or detector response methods. However, obviously energy spreading does occur. A chi-squared test can show exactly to what degree these two methods differ. The chi-squared statistic can be computed from

$$\chi^2 = \sum_{i=1}^{\infty} \left(\frac{N_{collision} - N_{detector}}{\sigma_{N,collision-N,detector}}\right)^2. \quad (5.3)$$

A reduced chi-squared can be determined from

$$\chi_\nu^2 = \frac{\chi^2}{\nu}. \quad (5.4)$$

Where ν is the number of degrees of freedom. The number of degrees of freedom can be determined from

$$\nu = n - f. \quad (5.5)$$

Where n is the number of position bins (MCA channels) and f is the number of fitting parameters. For this first analysis (difference in results between the PTRAC collision and detector response results) there are no fitting parameters. A lower value for χ_ν^2 indicates a better fit. Typically, a value less than 1 is considered the most desirable result.

Finally, a regression analysis for each of the test problems will be performed by first proposing a theoretical model for the detector response using the TALLYX substeps method. The theoretical model will include fitting parameters. Finding the optimal values for these parameters will consist of a simple Excel procedure involving the minimization of the reduced chi-squared value from Eq. (5.4).

5.1 Line Detector

The first problem run had a monoenergetic (thermal) $2.5 \cdot 10^{-8}$ MeV neutron source. This source was placed directly below the center of an 80 cm long (with a radius of 2.5 cm) BF_3 tube (gas only, no shell). The distance from the source to the tube was 40 cm and the rest of the problem was a vacuum. The source only emitted neutrons in the plane defined by a line running along the central axis of the gas volume and by a line going from the source to the centroid of the detector. A total of 10^8 source neutrons were simulated. The count data was sorted into 25 position bins. Figure 5.1 shows the position binning (with error bars) with all three methods while Figure 5.2 shows the difference between the two PTRAC methods.

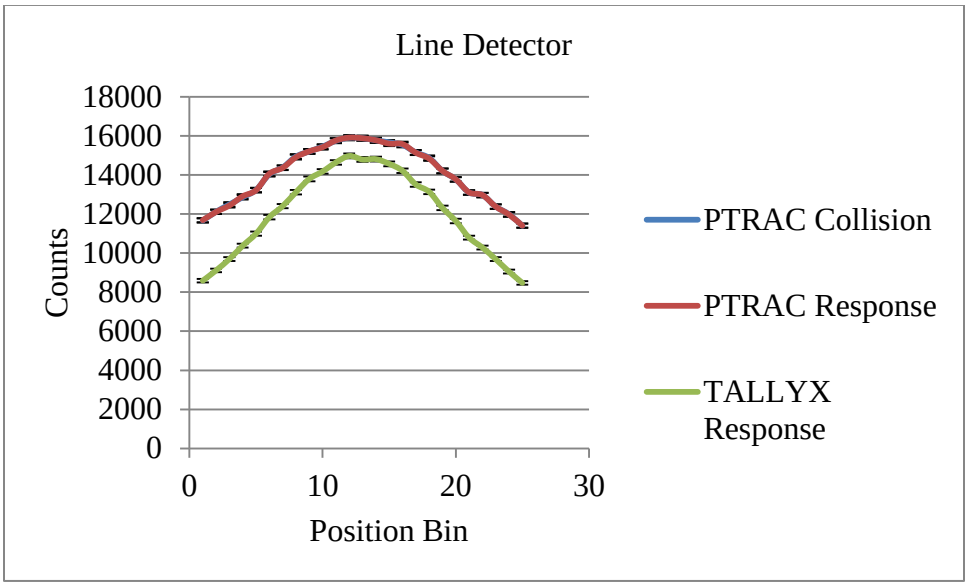

Figure 5.1: Counts and counting error results for all three methods (line detector).

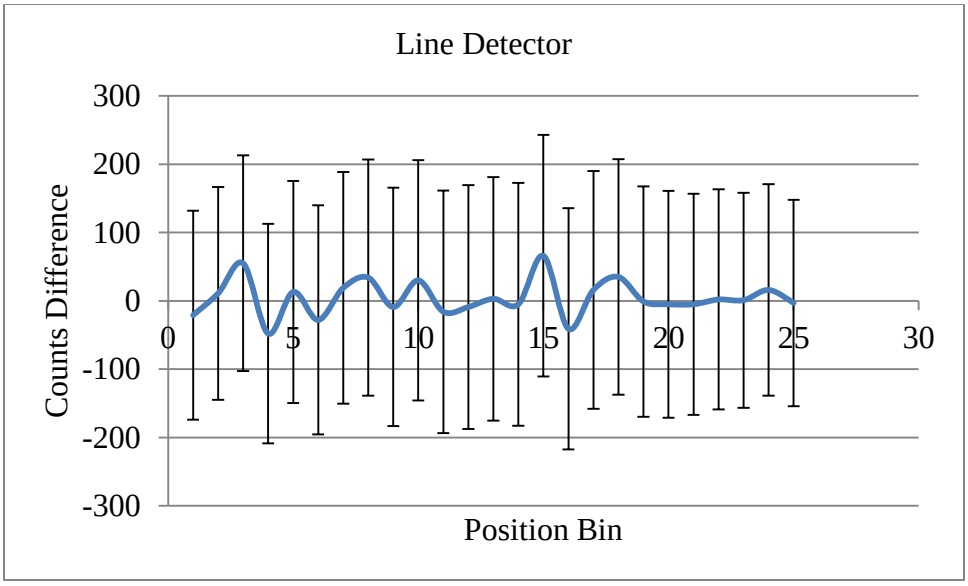

Figure 5.2: Counts difference between the two PTRAC methods (line detector).

From Figure 5.1 it is obvious that the PTRAC results match each very closely while the TALLYX results oddly reports a low total count of detected interactions. However, this is somewhat to be expected as these methods give different consideration when reporting pertinent events. A reduced chi-squared value for the data in Figure 5.2 gives a result of 0.126079608 indicating that the predicted detector response and the actual location of a neutron interaction are very close-there is only a minimal wall effect.

Because this is a line detector (the gas medium is assumed to be thin) an analytical expression exists for the position spectrum.

$$C = \frac{P}{s^2 + 1600}. \tag{5.6}$$

Where C is the number of counts in the bin, P is some fitting parameter and should be equal to the counts in the central position, and s is the distance (in cm) from the center of

a bin to the center of the central bin. Figure 5.3 shows a plot of the TALLYX results along with the fitted curve which resulted from chi-squared minimization.

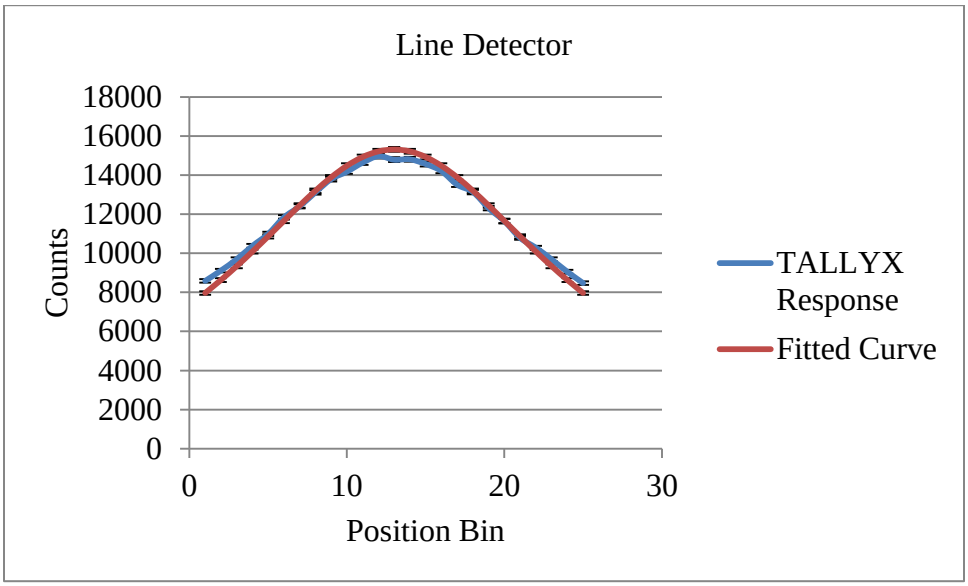

Figure 5.3: TALLYX curve fitting results (line detector).

The results from Figure 5.3 gave a result for the fitting parameter P to be 24504778.17 reduced chi-squared value of 9.814650108 which indicates a poor fit to the data as this is far greater than 1. Possible reasons for this include the fact that TALLYX records far fewer events than PTRAC for this problem, especially at the outermost position bins as seen in Figure 5.1. Additionally, the analytical solution from Eq. (5.6) is perhaps wrong. The detector is not exactly a line detector-it has some thickness and neutrons arriving in the outermost position bins actually travel through a larger thickness of the material, causing a higher number of interactions in those regions. The drop-off would be expected to be ½ moving from the central to outermost bins; however, the drop-off is much less than this.

5.2 Modified Localized Source Experiment

Another experiment analyzed was a localized source experiment. Figure 5.4 shows the arrangement for the detector tube but not the source used in this experiment.

Figure 5.4: BF_3 gas detector (much lower density than the simulations in Section 4.1) wrapped with an aluminum shell and wrapped in cadmium with a slit in the central portion of the tube. Reprinted from [16].

Not shown in Figure 5.4 is the fact that the neutron source was an AmBe mixed-field source wrapping in a moderating high density polyethylene material. This source-moderator component was placed directly over the opening in the cadmium wrapping. The total length of the aluminum tube was 91.44 cm and the opening in the slit was 0.3175 cm. While the neutron interactions would be expected to mostly concentrated within the area of the slit they would also appear in position bins outside of this region as well because the beam of neutrons entering the slit is not a collimated beam. However, because the slit is so far from the outermost bins, no large wall effect should be present. The remainder of the problem outside of what was described above is treated as vacuum. The count data was sorted into 288 position bins. Figure 5.5 shows the position binning

(with error bars) with all three methods while Figure 5.6 shows the difference between the two PTRAC methods.

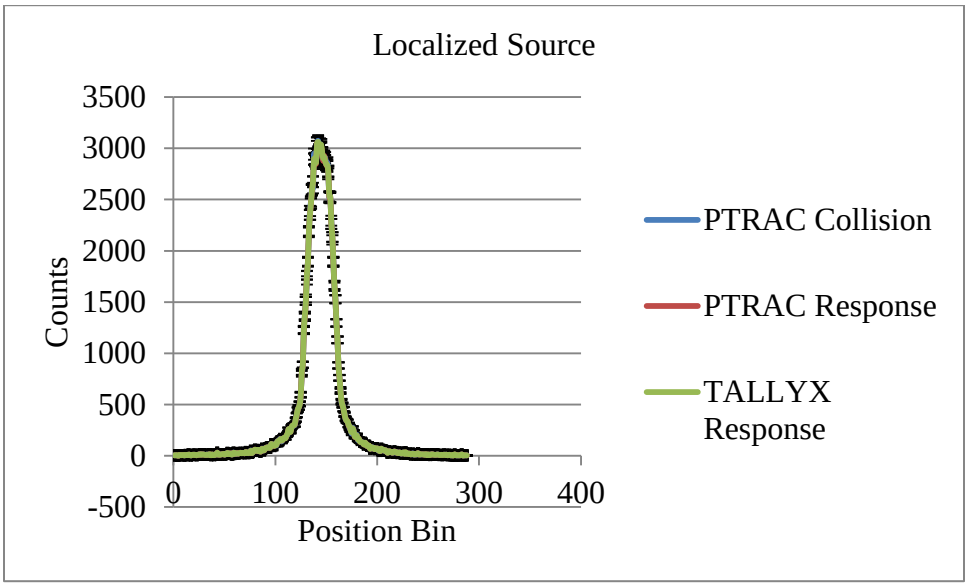

Figure 5.5: Counts and counting error results for all three methods (localized source).

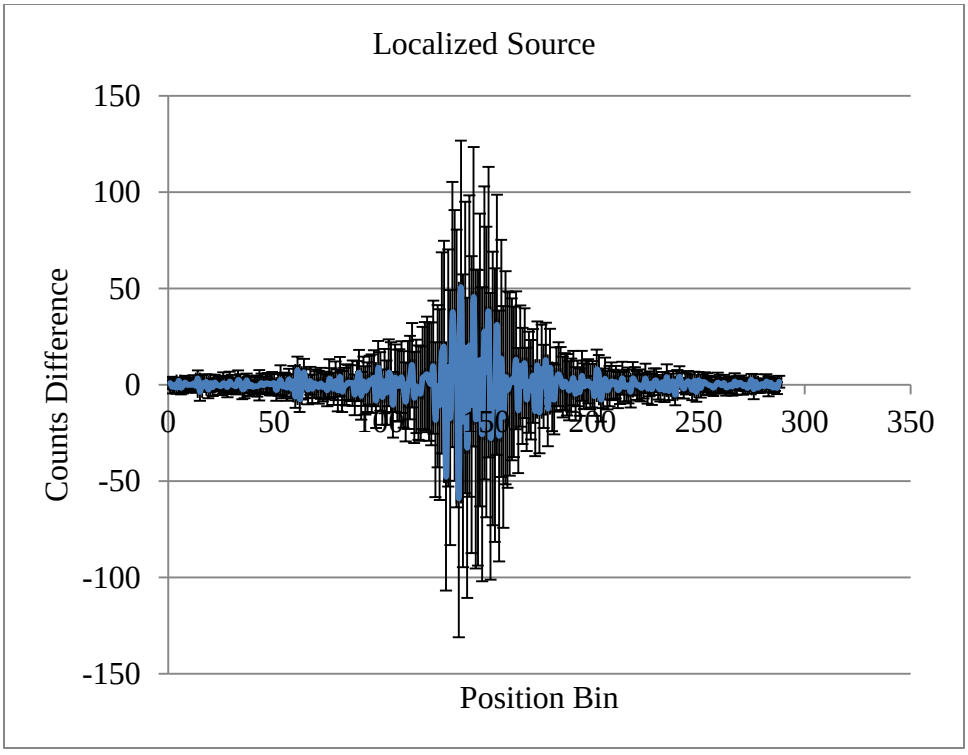

Figure 5.6: Counts difference between the two PTRAC methods (localized source).

From Figure 5.5 it is obvious that all three methods show much more congruency than for the problem described in Section 5.1. Specifically, the TALLYX method does not show significantly fewer counts than either of the two PTRAC methods. It is unknown why this occurs but a possible explanation may be this problem involves the use of a mixed-energy neutron source while the problem described in Section 5.1 has a monoenergetic neutron source. A reduced chi-squared value from the data in Figure 5.6 was computed to be 0.005652415. As this value is much less than 1 this indicates a good match between the two PTRAC methods and shows that as expected from a localization source experiment that there is no discernible wall effect.

Finally, a regression model was fit to the results from the TALLYX procedure. A Gaussian model with two fitting parameters was selected from a cursory look at the data from Figure 5.5.

$$C = Ae^{-\alpha s^2}. \tag{5.7}$$

Where A and α are fitting parameters. The reduced chi-squared value was determined to be 32.86812053 which is much higher than 1 and therefore not a very good result. This is most likely due to the fact there was a significant number of neutron interactions in the outer portion of the tube. Figure 5.7 shows a plot of the TALLYX results along with the fitted curve which resulted from chi-squared minimization.

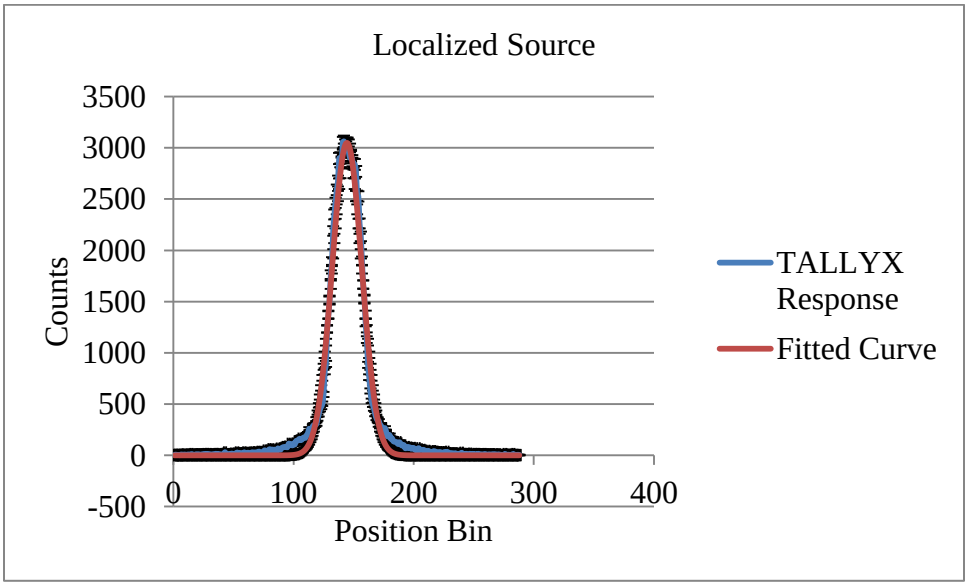

Figure 5.7: TALLYX curve fitting results (localized source).

The values for the fitting parameters A and α respectively were 3048.474144 and 0.032898382 respectively. Looking at Figure 5.7, it becomes obvious that a Gaussian is most likely not the correct choice for a curve fit. A Gaussian fit is too narrow given the simulated detector response. Most likely, there is a significant amount of backscattering

of neutrons within the detector tube which is leading neutron interactions outside of the area local to the source.

5.3 Modified Impurity Model (IM-1) Experiment

IM-1 was a series of experiments of high complexity which can not be accurately described here in words. These experiments involved using an AmBe mixed-field neutron source which then traversed through a large number of moderating materials in order to reach a spherical BF_3 detector which actually has the same gas density as the simulations from Section 4.1. An example of an IM-1 experiment (which was not actually the one simulated for this thesis) is shown in Figure 5.8.

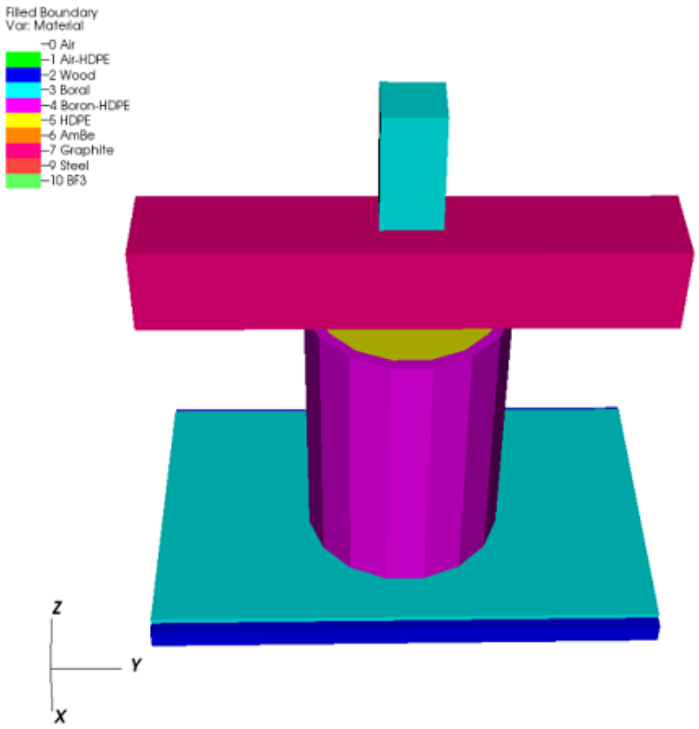

Figure 5.8: A representative example of an IM-1 experiment. Reprinted from [13].

The particular experiment in Figure 5.8 was analyzed in a large amount of detail by a previous graduate student. Figure 5.8 also provides a nice visualization how the spherical detector is covered by the boral shroud. In the experiment, the BF_3 detector was not position sensitive however for the purpose of the simulations it was assumed that the anode wire ran along the y-axis (referencing Figure 5.8) and through the center of the sphere. The count data was sorted into 5 position bins. Figure 5.9 shows the position binning (with error bars) with all three methods while Figure 5.10 shows the difference between the two PTRAC methods.

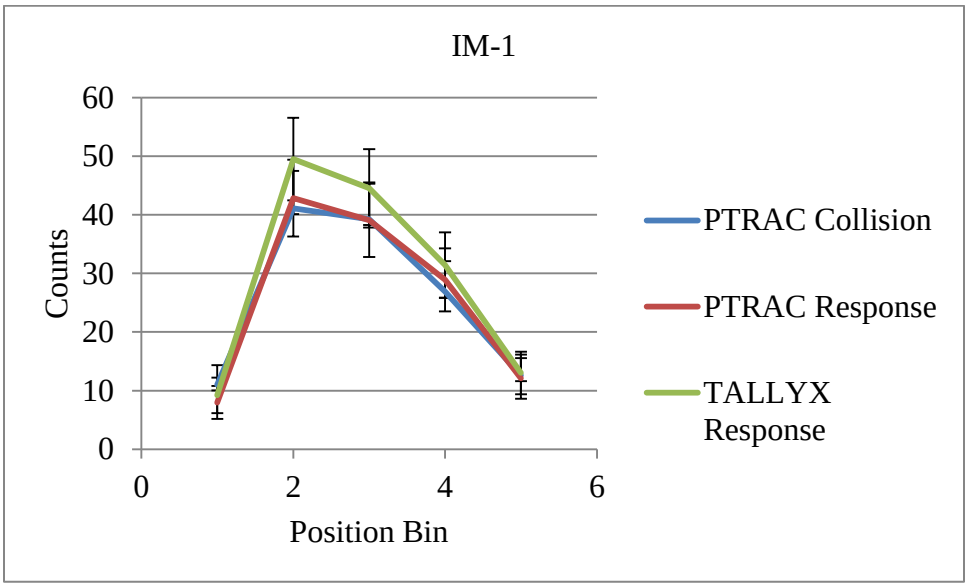

Figure 5.9: Counts and counting error results for all three methods (IM-1).

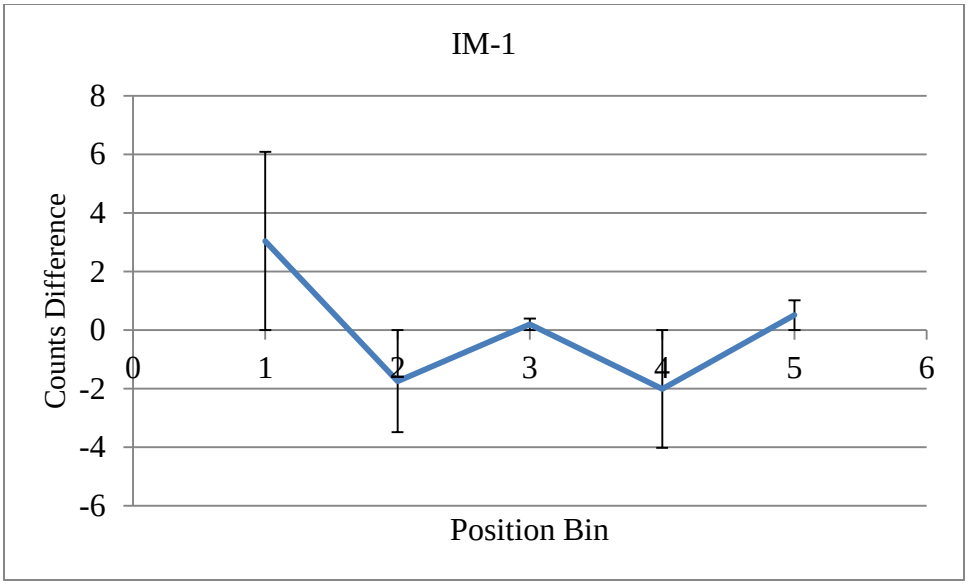

Figure 5.10: Counts difference between the two PTRAC methods (IM-1).

The value for the fitting parameter P is 139.3601073. From Figure 5.9 it is obvious that the TALLYX methods predicts a significantly higher number of total counts for this particle problem. Additionally, it appears from Figure 5.10 that this problem has a stronger wall effect than either of the problems from Section 5.1 or Section 5.2. However, the value for the reduced chi-squared given the data in Figure 5.10 is 0.121355946 which is much less than 1 and not significantly different from the results in either Section 5.1 or Section 5.2.

Finally, an analytical model of the position sensitive response can be determined because the position bins are equally spaced. Thus, the number of counts in bin can be determined to be:

$$C = PV. \tag{5.8}$$

Where P is a fitting parameter and V is the fraction of the sphere's volume that accounts for each position bin. From Figure 5.9 this seems like a good candidate for an analytic

solution-the position bins in the outer regions have far fewer counts. Figure 5.11 shows a plot of the TALLYX results along with the fitted curve which resulted from chi-squared minimization.

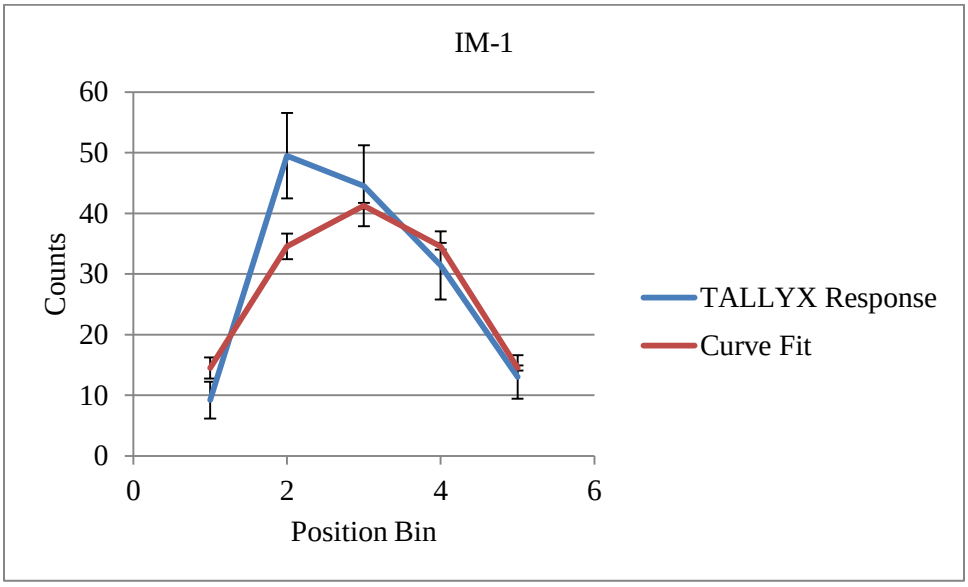

Figure 5.11: TALLYX curve fitting results (IM-1).

The chi-squared minimization results in a reduced chi-squared value of 2.072066681. This indicates a poor fit. However, given the asymmetry of the TALLYX result as seen in Figure 5.11 it is possible that this is due to simply not having enough total counts recorded. However, given the complexity of the problem as seen in the representative sample in Figure 5.8 this would be unwieldy and result in a simulation with perhaps too large of a computational expense. However, this was also the lowest reduced chi-squared of all analytical models proposed in either Section 5.1, Section 5.2, or Section 5.3. It is probably correct however the counts are too low. It should also be noted that Eq. (5.1) was used when computing all of the various errors; however, in some cases perhaps the number of counts was too low in order to apply Eq. (5.1).

6. CONCLUSIONS

Multiple methods were developed using the MCNP6 code in order to provide predictions for a the response of a 1D neutron PSD. However, there is some concern as to whether or not MCNP6 correctly models HCP's as well as it models electrons. Additionally, the PTRAC methods were consistent across all three of the test problems in that only a minimal wall effect was observed. This was surprising as the SR of alpha particles and ^{7}Li ions was found to be larger than the position bin size in some of these problems. Additionally, it was found that PTRAC and TALLYX did not even record the same events. There appears to be several possible reasons for this; however, due to the hidden nature of MCNP6's inner-workings it is not within the scope of this thesis to try and discover the reason for this discrepancy. Finally, none of the theoretical models matched any of the TALLYX results from each problem. This may been due to insufficient detail (backscattering of neutrons) or not enough counts or possible in the case of the problem described in Section 5.1 a TALLYX modification to a surface flux tally would have proved much more useful.

REFERENCES

[1] Crane, T.W., and M.P. Baker. “Neutron Detectors.” Passive Nondestructive Assay Manual. Los Alamos National Laboratory. http://www.lanl.gov/orgs/n/n1/panda/00326408.pdf

[2] Knoll, G.F. Radiation Detection and Measurement. 4th ed. New York: Wiley, 2010.

[3] Crawford, R.K. “Position-sensitive detection of slow neutrons-survey of fundamental principles.” Office of Scientific and Technical Information. 1992. https://www.osti.gov/scitech/servlets/purl/5095599-6rb0Q6/

[4] Convert, P. and J.B. Forsyth. “The Principles of Thermal Neutron Production,” and “An Introduction to the Types of Position-sensitive Neutron Detectors.” Position-Sensitive Detection of Thermal Neutrons. Eds. Convert, P. and J.B. Forsyth. New York: Academic Press, 1983. 1-46.

[5] D.B. Pelowitz, Ed., "MCNP6 Users Manual Version 1.0" LA-CP-13-00634 (2013).

[6] Solomon, C.J. “A Patch to MCNP5 for Multiplication Interference: Description and User Guide” LA-UR-14-23160 (2011).

[7] Stevenson, A.W. *Improving the Efficiency of Photon Collection By Compton Rescue.* MS Thesis, Air Force Institute of Technology, 2011. http://www.dtic.mil/dtic/tr/fulltext/u2/a538792.pdf

[8] Turner, J.E. Atoms, Radiation, and Radiation Protection. 3rd edition. Wiley-VCH: Weinheim, 2008. 109-137.

[9] Frame, P. “Boron Trifluoride (BF3) Neutron Detectors.” Oak Ridge Associated

Universities. 1999. https://www.orau.org/ptp/collection/proportional%20counters/bf3info.htm

[10] de Almeida, M. and M. Moralles. “Monte Carlo simulation of a position sensitive gamma ray detector.” Brazilian Journal of Physics, 2005. http://www.scielo.br/pdf/bjp/v35n3b/a04v353b.pdf

[11] Spieler, H. “Position-Sensitive Detectors.” University of California, Berkeley, 1998. http://www-physics.lbl.gov/~spieler/physics_198_notes/PDF/VI-PSD.pdf

[12] Tesinsky, M. “MCNPX Simulations for Neutron Cross Section Measurements.” MS Thesis, Royal Institute of Technology, 2010. ftp://ftp.nrg.eu/pub/www/talys/tendl2010/presentations/TesinskyMilan.pdf

[13] Ghaddar, T. *Load Balancing Unstructured Meshes For Massively Parallel Transport Sweeps.* MS Thesis, Texas A&M University, 2016. http://oaktrust.library.tamu.edu/bitstream/handle/1969.1/157129/GHADDAR-THESIS-2016.pdf?sequence=1&isAllowed=y

[14] M.B. Chadwick, M. Herman, P. Obložinský, M.E. Dunn, Y. Danon, A.C. Kahler, D.L. Smith, B. Pritychenko, G. Arbanas, R. Arcilla, R. Brewer, D.A. Brown, R. Capote, A.D. Carlson, Y.S. Cho, H. Derrien, K. Guber, G.M. Hale, S. Hoblit, S. Holloway, T.D. Johnson, T. Kawano, B.C. Kiedrowski, H. Kim, S. Kunieda, N.M. Larson, L. Leal, J.P. Lestone, R.C. Little, E.A. McCutchan, R.E. MacFarlane, M. MacInnes, C.M. Mattoon, R.D. McKnight, S.F. Mughabghab, G.P.A. Nobre, G. Palmiotti, A. Palumbo, M.T. Pigni, V.G. Pronyaev, R.O. Sayer, A.A. Sonzogni, N.C. Summers, P. Talou, I.J. Thompson, A. Trkov, R.L. Vogt,

S.C. van der Marck, A. Wallner, M.C. White, D. Wiarda, P.G. Young, "ENDF/B-VII.1: Nuclear Data for Science and Technology: Cross Sections, Covariances, Fission Product Yields and Decay Data", Nucl. Data Sheets 112(2011)2887.

[15] Ziegler, J.F., and Manoyan, J.M. “The Stopping of Ions in Compounds.” Nuclear Instruments and Methods in Physics Research B35, 1988, 215-228. http://www.sciencedirect.com/science/article/pii/0168583X8890273X

[16] Pongpun, Sophit. “BF3 Cylindrical Tube Preliminary Test Results Data Acquisition Date: May 19, 2017.” Internal report. 13 June 2017.